Frontiers of Information Technology & Electronic Engineering
www.jzus.zju.edu.cn; engineering.cae.cn; www.springerlink.com
ISSN 2095-9184 (print); ISSN 2095-9230 (online)
E-mail: jzus@zju.edu.cn

Correspondence:

Wavelength-selective wavefront shaping by metasurface*#

Zixin CAI[§1], Xin HE[†‡§1], Xin LIU[1], Shijie TU[1], Xinjie SUN[1], Paul BECKETT[2], Aditya DUBEY[3], Arnan MITCHELL[3], Guanghui REN[†‡3], Xu LIU[1], Xiang HAO[†‡1,4,5]

[1]*State Key Laboratory of Modern Optical Instrumentation, College of Optical Science and Technology, Zhejiang University, Hangzhou 310027, China*

[2]*School of Engineering, RMIT University, Melbourne 3000, Australia*

[3]*Integrated Photonics and Applications Centre (InPAC), RMIT University, Melbourne 3001, Australia*

[4]*Intelligent Optics & Photonics Research Center, Jiaxing Research Institute Zhejiang University, Jiaxing 314000, China*

[5]*Jiaxing Key Laboratory of Photonic Sensing & Intelligent Imaging, Jiaxing 314000, China*

[†]E-mail: xinhe.wins@outlook.com; guanghui.ren@rmit.edu.au; haox@zju.edu.cn

Received Oct. 25, 2022; Revision accepted Jan. 3, 2023; Crosschecked Mar. 24, 2023

https://doi.org/10.1631/FITEE.2200510

Precise, wavelength-dependent phase retarding is essential in many fields, such as superresolution imaging, full-color holography, nanomanufacturing, and optical communications. This demand can be achieved by a combination of multiple optical devices but is challenging to implement using a single element. In this paper, we develop a method for metasurface design that allows wavelength-selective wavefront shaping. Specifically, we demonstrate a metasurface that can selectively modulate a beam with a spiral phase at 785 nm and leave another beam unaffected at 590 nm. The wavefronts are experimentally validated by an interferometer and the measurement of the corresponding point spread functions (PSFs). Compared to prior spatial multiplexing and dispersion engineering approaches, our strategy is straightforward and flexible during optimization for systems that need to selectively modulate one beam at a wavelength and leave another one unaffected. Such a planar device provides a compact method for wavelength-selective wavefront modulation.

1 Introduction

Phase modulation is demanding across a range of applications, such as optical communication (Huang et al., 2020), superresolution imaging (Hell and Wichmann, 1994; Hao et al., 2021), beam shaping (Ouadghiri-Idrissi et al., 2016), quantum cryptography (Mirhosseini et al., 2015), and holographic displays (Sasaki et al., 2014). Conventional approaches to phase modulation involve devices such as phase plates (Ruffato et al., 2014; Guo et al., 2020), deformable mirrors (Ma et al., 2018; Yu et al., 2018), and spatial light modulators (Jesacher et al., 2014; Liu X et al., 2021, 2022), which allow flexible wavefront shaping. However, they are always bulky and tend to dramatically

§ These two authors contributed equally to this work

‡ Corresponding authors

* Project supported by the "Leading Goose" Research and Development Program of Zhejiang Province, China (No. 2022C01077), the National Key Research and Development Program of China (No. 2018YFA0701400), the National Natural Science Foundation of China (No. 92050115), the Zhejiang Provincial Natural Science Foundation of China (No. LZ21F050003), the Fundamental Research Funds for the Central Universities, China (No. 226-2022-00137), and the Zhejiang Postdoctoral Science Fund for Excellent Project (No. 511300-X82101)

Electronic supplementary materials: The online version of this article (https://doi.org/10.1631/FITEE.2200510) contains supplementary materials, which are available to authorized users

ORCID: Zixin CAI, https://orcid.org/0009-0001-2076-5997; Xin HE, https://orcid.org/0000-0002-5843-0332; Guanghui REN, https://orcid.org/0000-0002-9867-8279; Xiang HAO, https://orcid.org/0000-0002-3931-6884

increase the system's complexity when multiple laser beams with diverse wavefronts are expected.

Metasurfaces, comprising surface-patterned nanostructures with subwavelength geometries, have attracted much attention in recent years due to their excellent light modulation capability. These nanoscale patterned surfaces have been shown to interact with the modulated incident wavefront in terms of polarization (Mueller et al., 2017; Liu MZ et al., 2021; Zheng et al., 2021), angle of incidence (Deng et al., 2018; Spägele et al., 2021), and wavelength (He et al., 2020; Zhang et al., 2021) multiplexing. In particular, compared to conventional optical devices, metasurface structures show unprecedented flexibility to manipulate the properties of light, leading to various ultrathin optical elements, such as metalenses (Khorasaninejad et al., 2016b), holographic pulse shapers (Georgi et al., 2021), vortex beam generators (Hu et al., 2021), and filters (Yang et al., 2020).

Among them, wavelength-selective metasurfaces exhibit the additional ability to implement distinct modulation functions at different illumination wavelengths. Previous studies on wavelength-selective metasurfaces include sectoring regions (Khorasaninejad et al., 2016a; Maguid et al., 2016; Li et al., 2021), interleaved pixels (Arbabi et al., 2016; Bao et al., 2019; Feng et al., 2019), and dispersion engineering of subwavelength building blocks (Sell et al., 2017; Shi et al., 2018; Shrestha et al., 2018). In sectoring and interleaved approaches, the metasurface is divided into several regions or subpixels, each specifically aiming at a unique wavelength. Owing to their partitioned geometry, these spatial multiplexing approaches inevitably suffer from crosstalk problems between adjacent regions or subpixels. They also exhibit an inherent limit to their maximum efficiency since each subregion is designed for only one wavelength. In contrast, dispersion engineering approaches can simultaneously fulfil the target wavefront modulation at all desired wavelengths, thereby addressing the crosstalk issue and overcoming the transmission efficiency limit. However, these methods require building a large meta-atom library to meet the multiwavelength response and thus mandate a brute-force search of all these potential building blocks, which in turn requires huge computing resources. This presents an increasing design and optimization challenge as the number of operating wavelengths increases.

In this paper, we employ a combination of wavelength-dependent polarization conversion and geometric phase (Mueller et al., 2017) to design a metasurface-based wavelength-selective phase modulator that can exhibit unique wavefront responses at different illumination wavelengths. Specifically, we design a metasurface that focuses the beam to an annular ring at 785 nm and a solid spot at 590 nm. For those systems that need to selectively modulate one wavelength wavefront and leave another unaffected, our design can break the inherent efficiency limit since every element simultaneously contributes at both target wavelengths in contrast to the spatial multiplexing approaches. Furthermore, brute-force searching of the unit cell in a large meta-atom library is not required so that the optimization process is less time-consuming.

2 Design and simulation

The basic building block of our design, shown in Fig. 1a, consists of a rectangular nanofin arranged on a hexagonal substrate with the center-to-center distance S. Each nanofin has the same height (H), length (L), and width (W), but has different azimuthal angles φ's at different positions. Such an element can be described as a conventional linearly birefringent waveplate with the Jones matrix $\boldsymbol{J}(\varphi)$ (Devlin et al., 2016):

$$\boldsymbol{J}(\varphi)=\boldsymbol{R}(-\varphi)\begin{bmatrix}\tilde{t}_{\mathrm{l}} & 0\\ 0 & \tilde{t}_{\mathrm{s}}\end{bmatrix}\boldsymbol{R}(\varphi), \tag{1}$$

where $\boldsymbol{R}(\varphi)$ is the rotation matrix and $\tilde{t}_{\mathrm{l}}$ and $\tilde{t}_{\mathrm{s}}$ are the complex transmission coefficients along the long and short axes of the nanofin, respectively. With a circularly polarized beam incidence, the transmitted beam can be expressed as

$$\boldsymbol{T}(\varphi)=\boldsymbol{J}(\varphi)\begin{bmatrix}1\\ \pm\mathrm{i}\end{bmatrix}=\frac{\tilde{t}_{\mathrm{l}}+\tilde{t}_{\mathrm{s}}}{2}\begin{bmatrix}1\\ \pm\mathrm{i}\end{bmatrix}+\frac{\tilde{t}_{\mathrm{l}}-\tilde{t}_{\mathrm{s}}}{2}\mathrm{e}^{\pm\mathrm{i}2\varphi}\begin{bmatrix}1\\ \mp\mathrm{i}\end{bmatrix}, \tag{2}$$

which shows that the transmitted beam includes two components: the copolarization part and the cross-polarization part. The modulated phase shift of the copolarization part includes only the dynamic phase (the phase part of $\frac{\tilde{t}_{\mathrm{l}}+\tilde{t}_{\mathrm{s}}}{2}$), also called the propagation

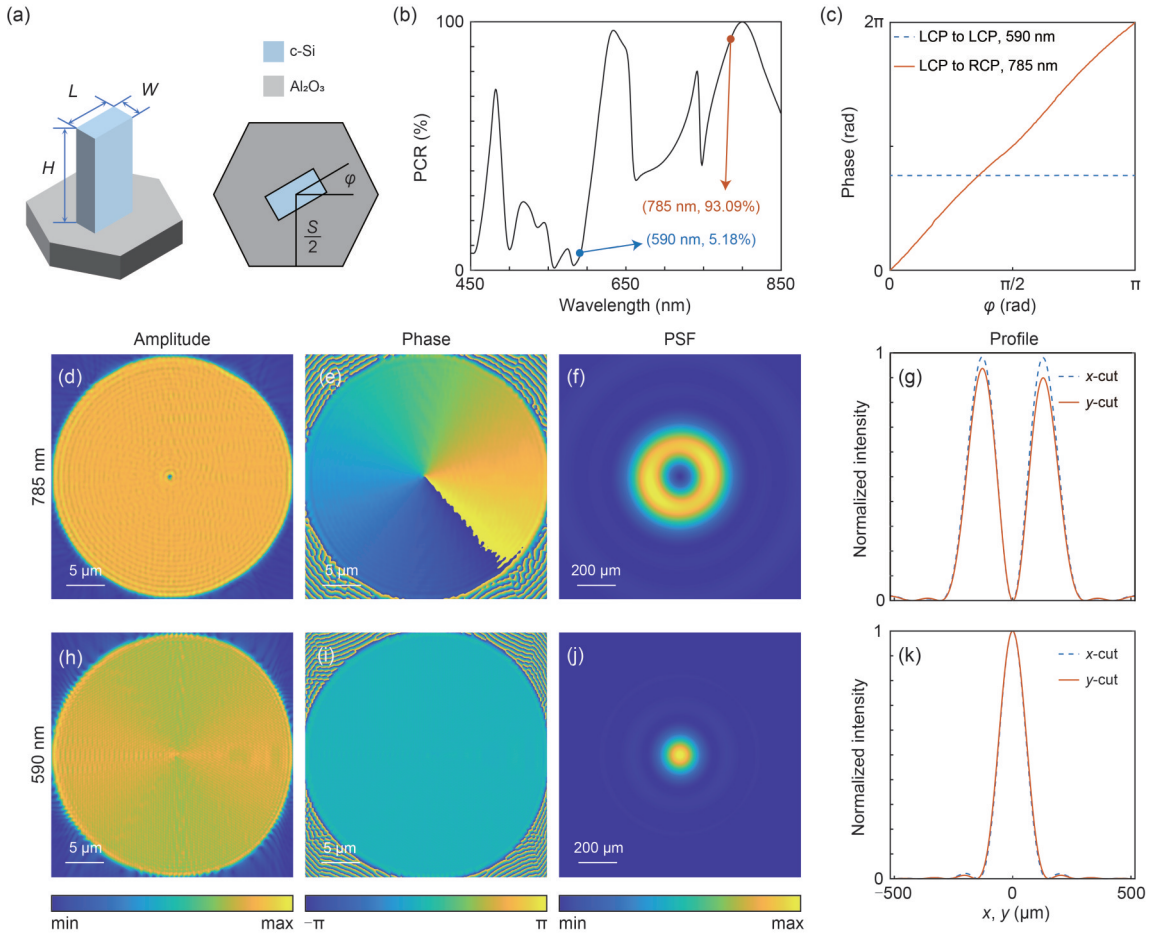

Fig. 1 Metasurface design and simulation validation

(a) is the schematic of a unit cell of the metasurface; (b) is the simulated polarization conversion rate (PCR) of the unit cell (L=185 nm and W=83 nm); (c) is the simulated phase delay of the transmitted beam as a function of φ at different wavelengths with opposite polarizations; (d) and (e) are the simulated near-field amplitude and phase distribution at 590 nm, respectively; (h) and (i) are the simulated near-field amplitude and phase distribution at 785 nm, respectively; (f) and (j) refer to the corresponding simulated point spread function (PSF) results at different wavelengths based on near-field data, while with the amplitude and phase distribution, an annular PSF and a solid PSF can be obtained; (g) and (k) refer to the intensity profiles along the horizontal and vertical lines cutting through the center of the PSFs, respectively (LCP: left circular polarization; RCP: right circular polarization)

phase, which is a function of the nanofin material and its geometry. In addition to this propagation phase, the phase shift of the cross-polarization includes another component: the Pancharatnam–Berry (PB) phase, also called the geometric phase, which is a function of the azimuthal angle φ for the nanofin (Berry, 1987). An important difference here is that while the propagation phase is wavelength-dependent and determined by the fin size, the PB phase is affected only by its azimuthal angle and is independent of its size. Once the length L and the width W are fixed, so are the complex transmission coefficients $\tilde{t}_l$ and $\tilde{t}_s$, as well as the propagation phase of two beams with different circular polarization values. Thus, while the PB phase remains fixed unless the azimuthal angle is changed, the nanofin size affects the complex transmission coefficients and therefore affects the output polarization state of the transmitted beam. As a result, by suitably designing the size, a low polarization conversion rate (PCR) (mainly copolarization part with only propagation phase) at the desired wavelength and a high PCR (mainly cross-polarization part with propagation phase and PB phase) at another specified wavelength can be obtained. Here, PCR is defined as the ratio of the transmitted optical power with the opposite helicity to the total transmitted power. Based on this concept,

a fixed phase shift of the copolarization part can be obtained according to Eq. (1) at a given wavelength. To generate an annular-shaped PSF at another wavelength, the metasurface would have to impose a spiral phase on the incident beam, which can be achieved by rotating the nanofin to set the PB phase of the cross-polarization component.

As a demonstration, we explored the operation of the metasurface at two wavelengths: a constant phase modulation at 590 nm and a spiral phase modulation at 785 nm. As the propagation phase in Eq. (2) depends on the nanofin material and its geometry, the selection of the metasurface material is an important design choice. We used crystalline silicon (c-Si) in this demonstration due to the low extinction coefficient of its transparent window across the visible and near-infrared (NIR) regions (Ikezawa et al., 2022). First, we simulated the unit cell of our design using the COMSOL Multiphysics finite element analysis tool to find suitable fin dimensions. In the simulation, periodic boundary conditions were applied at x and y boundaries, and perfectly matched layers were applied at z boundary. To satisfy the Nyquist sampling criterion and suppress high-order diffraction effects, the center-to-center distance S was set to 400 nm. A nanofin height (H) of 500 nm was found to optimize transmission properties at the two wavelengths. The width (W) and length (L) were determined to maximize PCR at a wavelength of 785 nm and minimize PCR at 590 nm. Fig. 1b shows that a nanofin with W= 93 nm and L=185 nm can provide the desired PCR at the two target wavelengths. At 785 nm, the transmitted beam comprises just over 93% of the cross-polarization component, while at 590 nm, the copolarization component dominates at over 90%. The transmission efficiency is approximately 58% at 590 nm and 98% at 785 nm. Fig. 1c shows the phase shift with different rotation angles at different wavelengths. At 785 nm, the phase shift of the cross-polarization part is twice the azimuthal angle, while the phase shift of the copolarization part is constant at 590 nm. The spiral phase distribution p at 785 nm can be expressed as follows:

$$p(r,\theta) = q\theta, \tag{3}$$

where (r, θ) are the cylindrical coordinates of each nanofin on the metasurface and q is the topological charge. Thus, combined with Eq. (2), the azimuthal angle of each nanofin is

$$\varphi(r,\theta) = \frac{q}{2}\theta. \tag{4}$$

In our case, we set the topological charge q to ±1, where the sign depends on the handedness of the incident circular polarization. The simulation of the overall device was performed using commercial finite-difference time-domain software (FDTD solutions, Lumerical Inc.). The diameter of the metasurface was set to 36 μm due to the computational cost concerns. In contrast to the simulation of the unit cell, perfectly matched layers were used at x, y, and z boundaries. An x-polarized plane-wave source with its phase set to 0° and a y-polarized plane-wave source with its phase set to 90° were used to build a circularly polarized incident beam. A perfect electrical conductor (PEC) aperture was set to match the diameter of our design and filter the unmodulated beam.

As shown in Figs. 1d and 1h, the simulated amplitude distributions of the two wavelengths are almost uniform. The corresponding phase distribution results are given in Figs. 1e and 1i. The results exhibit a spiral phase distribution at 785 nm and a relatively flat phase distribution at 590 nm. After being modulated by the metasurface, the incident beam can then be focused to an annular PSF (Fig. 1f) and a solid PSF (Fig. 1j). These PSFs are calculated according to the vectorial diffraction theory described by Richards and Wolf (1959) and Liu X et al. (2021). Finally, the intensity profiles along the horizontal and vertical lines cutting through the center of the PSFs are shown in Figs. 1g and 1k, respectively.

3 Fabrication and results

To physically verify our design, a circular metasurface with a diameter of 500 μm was fabricated on a crystalline silicon-on-sapphire (SOS) wafer (Section 1 in the supplementary materials for details of fabrication). Both optical and scanning electron microscopy (SEM) images of the fabricated metasurface are shown in Fig. 2. In this section, we will discuss the performance of the metasurface from the phase distribution to the PSF results.

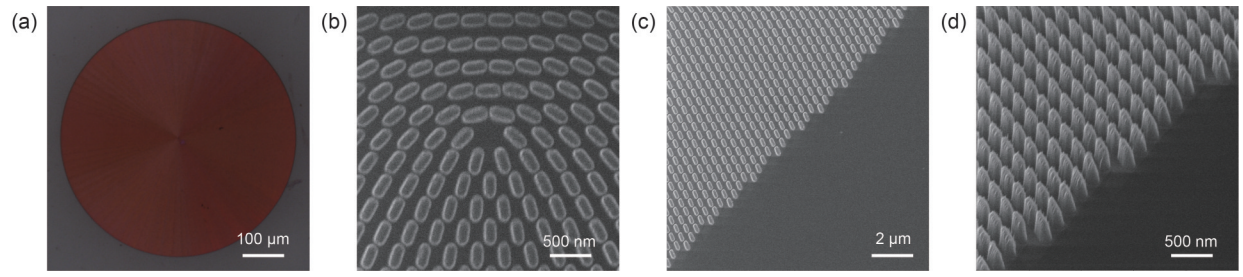

Fig. 2 Optical image and scanning electron microscopy (SEM) image of the fabricated metasurface, comprising c-Si nanofins on an Al_2O_3 substrate: (a) optical image of the metasurface; (b) top-view image of the center portion of the fabricated metasurface; (c) top-view image of the edge portion of the fabricated metasurface; (d) side-view image of the metasurface

To characterize the spiral phase distribution, we used a custom-built Mach–Zehnder interferometer as shown in Fig. 3a (Section 2 in the supplementary materials for details of the configuration). The orientation of the Al_2O_3 substrate we used is r-plane (1-102), and the thickness is 530 μm. As the substrate is anisotropic, the linearly polarized beam should first be turned into an elliptically polarized beam (inset in Fig. 3a). The Al_2O_3 substrate then imposes circular polarization in a direction opposite to that of the reference beam. Thus, the rotation angle of the second quarter-wave plate (QWP2) in front of the metasurface must be carefully designed to alleviate the systematic error of the wavefront measurement. This can be determined by observing the interference fringe in the unmodulated area outside the metasurface. As shown in Figs. 3b and 3c, the background outside the perimeter of the metasurface does not interfere with the reference beam only when the QWP2 and the Al_2O_3 substrate modulate the linearly polarized incident beam into circular polarization. Meanwhile, the interference fringe in the area of the metasurface achieves the highest contrast, which can serve to increase the precision of the phase retrieval. If the wave plate is not at the correct rotation angle, the background will interfere with the reference beam because of its elliptical polarization, as shown in Figs. 3d and 3e. In this way, the correct polarization of the incident beam can be confirmed. Fig. 3f shows the forked interference fringe captured by the camera at 785 nm. Then, the wavefront is extracted via the Fourier transform-based method (Zhao et al., 2021), as shown in Fig. 3g. The observed phase is close to the simulated phase in Fig. 1e and thus agrees well with our theoretical prediction. To quantify the quality of the phase, we calculated the error between the measured phase and the standard phase. The result (Fig. 3h) shows an almost uniform distribution, indicating that the measured phase distribution closely matches the target spiral phase. In addition, the root mean square (RMS) wavefront error is 0.2789.

Although the shape of the annular PSF is determined mainly by the phase distribution, other factors, such as amplitude and polarization, are still considered. To quantify the effect, we directly characterized the PSF at different wavelengths. The setup is available in Fig. S2 in the supplementary materials. Since the size of the metasurface is small, here we used a 4*f* system to match the pupil size of the aperture that filters out the unmodulated beam. As presented in Figs. 3i and 3j, an annular PSF at 785 nm and a solid PSF at 590 nm are obtained, thereby verifying our initial design. Fig. 3k shows the intensity profiles at different wavelengths across horizontal and vertical transects. At 785 nm, the transmitted beam consists almost entirely the cross-polarization component with spiral phase modulation. At 590 nm, a Gaussian beam profile is observed, which means that the beam consists primarily of the copolarization component without spiral phase modulation. A polarimeter was used to obtain the Jones vector of the transmitted beam, and the PCR was calculated from the vector. The result is approximately 91% at 785 nm and 8% at 590 nm. These results illustrate that our design can modulate the beam with different phase modulations at different wavelengths, one with spiral phase modulation and the other with a relatively flat phase shift. The beam can then be focused into either an annulus or a spot.

From the measured PSF profile shown in Fig. 3k, the *x*- and *y*-transect plots are slightly different from each other, which may have been caused by aberration and irregular illumination. Furthermore, the minimum

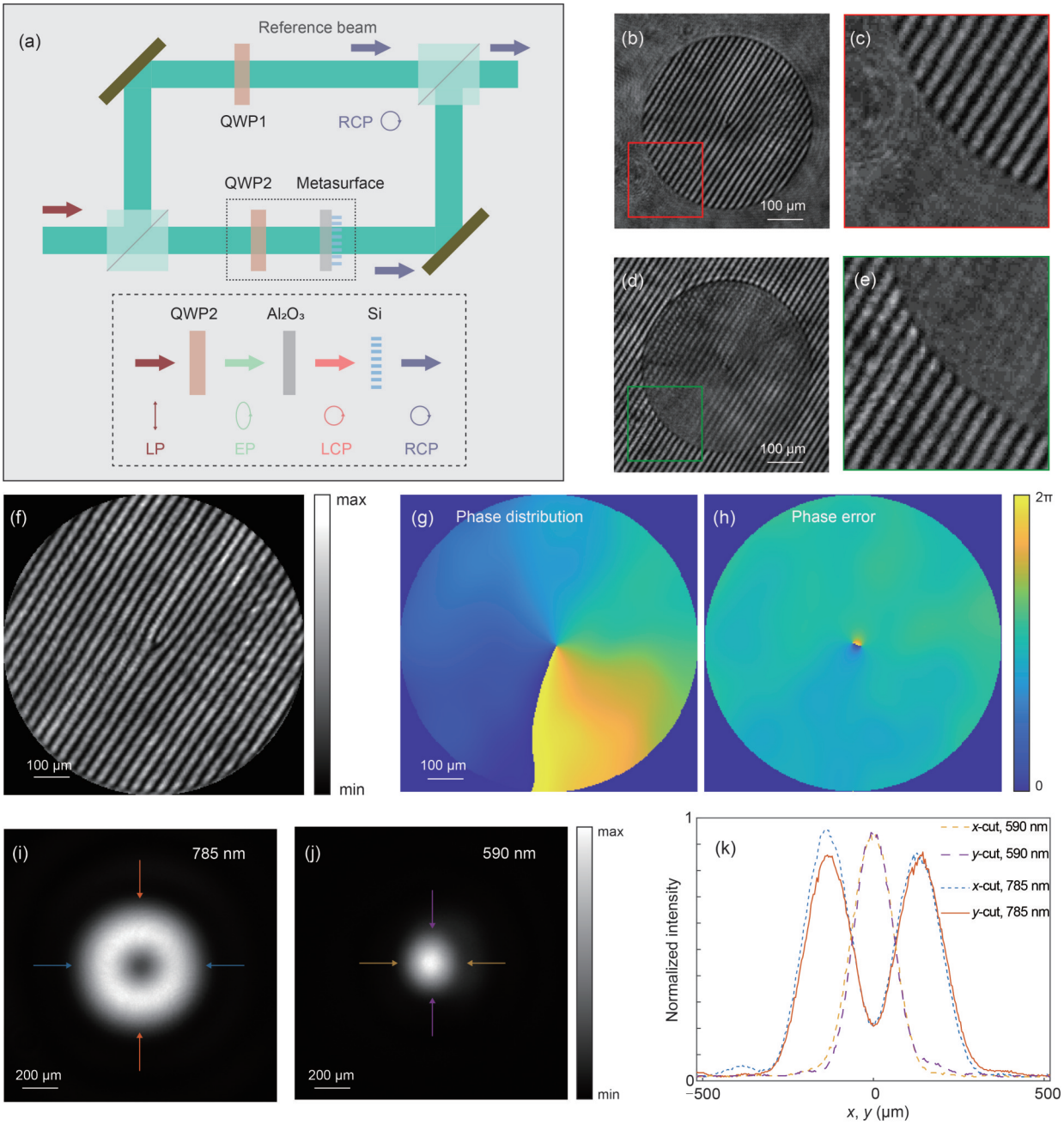

Fig. 3 Characterization of the designed metasurface

(a) is the schematic of the Mach–Zehnder interferometer for spiral phase modulation; (b) and (d) refer to the interference fringe with the quarter-ware plate (QWP) at different rotation angles; (c) and (e) refer to the areas in the red and green squares, respectively; (f) is the interference fringe of the modulated beam; (g) is the measured spiral phase distribution of the metasurface; (h) is the error between the measured phase distribution and the standard spiral phase distribution; (i) and (j) refer to the measured point spread function (PSF) of the modulated beams at 785 nm and 590 nm, respectively; (k) shows the intensity profiles at different wavelengths across horizontal areas and vertical transects (References to color refer to the online version of this figure)

at the center of the PSF is nonzero (i.e., slightly over 20% of the peak in Fig. 3k), which is different from the simulation result. This can be explained by the fact that the geometric size of the nanofin (shown in Fig. 2) does not perfectly match the designed geometry due to fabrication error, leading to a lower PCR and introducing some copolarized noise to the annular PSF. It is possible to circumvent this limitation by advanced

manufacturing technology. In addition, it is possible to improve the transmission performance by using a SiO_2 substrate instead of Al_2O_3 but at the expense of a more complex manufacturing process (Bao et al., 2019). Since the SiO_2 substrate does not change the polarization state of the incident beam, as does the Al_2O_3 substrate, it can reduce the difficulty of using the metasurface without an elliptically polarized incident beam.

Although the spiral phase modulation of the metasurface is designed for a single wavelength, the metasurface still performs adequately over a reasonably wide range of wavelengths. As shown in Fig. 4, a Gaussian PSF can be obtained at 545 nm, 555 nm, 565 nm, and 575 nm, while a clear annulus is still visible at 645 nm, 705 nm, 755 nm, and 795 nm. This can be explained by noting that the device has a low PCR between 545 nm and 575 nm, as shown in Fig. 1b; thus, the transmitted beam consists mainly of the copolarization component with constant phase modulation. For other wavelengths, the device has a high PCR, and the transmitted beam consists mainly of the cross-polarization component with spiral phase modulation. Although the contrast between the bright and dark regions varies nonmonotonically and may not be sufficient for some applications, these results indicate that it would be straightforward to expand the design to other combinations of wavelengths or even to multiwavelength configurations.

4 Conclusions

In summary, we have proposed a wavelength-selective shaping metasurface based on a combination of wavelength-dependent polarization conversion and geometric phase modulation. To verify the theory, we designed and fabricated a metasurface that can modulate an incident beam with a spiral phase at 785 nm and another with a relatively flat phase at 590 nm. The beams can then be focused into either an annular or a solid PSF depending on the wavelength, which may be useful for photolithographic systems, stimulated emission depletion (STED) microscopy systems, and other applications where auto-alignment of the beam is demanded. This scheme can also be expanded to any other combination of wavelengths or multiwavelength configurations. This ultracompact wavelength-selective device is a promising building block in the development and integration of complex optical systems.

Contributors

Zixin CAI, Xin HE, Xu LIU, and Xiang HAO designed the research. Zixin CAI and Xin HE processed the data, performed the theoretical analysis and the measurement of the sample, and

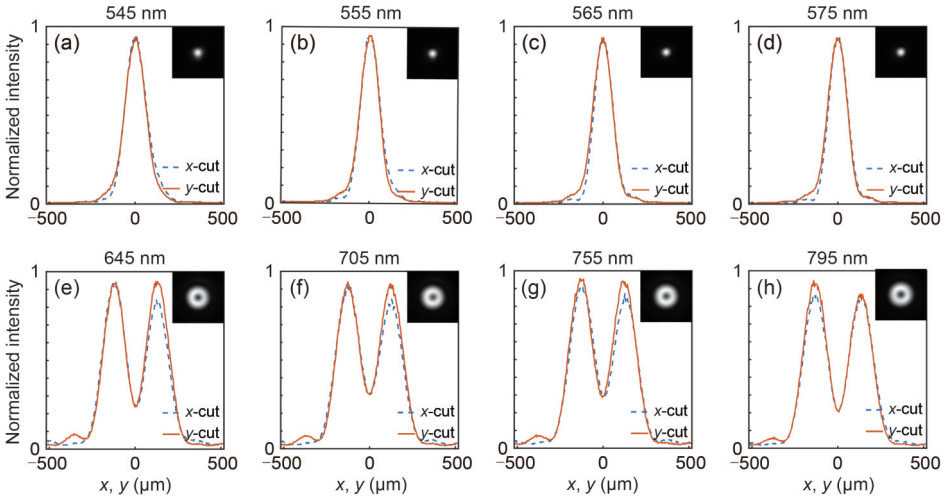

Fig. 4 Measured point spread functions (PSFs) and the intensity profile across horizontal and vertical transects at different wavelengths

First row: solid spot PSFs with low polarization conversion rate (PCR) at 545 nm (a), 555 nm (b), 565 nm (c), and 575 nm (d); second row: annular PSFs with high PCR at 645 nm (e), 705 nm (f), 755 nm (g), and 795 nm (h). Inset: the corresponding measured PSFs at different wavelengths

drafted the paper. Aditya DUBEY, Arnan MITCHELL, and Guanghui REN fabricated the samples. Xin LIU, Shijie TU, Xinjie SUN, and Paul BECKETT helped organize the paper. Zixin CAI, Xin HE, and Xiang HAO revised and finalized the paper.

Acknowledgements

We thank the Westlake Center for Micro/Nano Fabrication for facility support and technical assistance.

Compliance with ethics guidelines

Zixin CAI, Xin HE, Xin LIU, Shijie TU, Xinjie SUN, Paul BECKETT, Aditya DUBEY, Arnan MITCHELL, Guanghui REN, Xu LIU, and Xiang HAO declare that they have no conflict of interest.

Data availability

The data that support the findings of this study are available from the corresponding authors upon reasonable request.

References

Arbabi E, Arbabi A, Kamali SM, et al., 2016. Multiwavelength metasurfaces through spatial multiplexing. *Sci Rep*, 6:32803. https://doi.org/10.1038/srep32803

Bao YJ, Yu Y, Xu HF, et al., 2019. Full-colour nanoprint-hologram synchronous metasurface with arbitrary hue-saturation-brightness control. *Light Sci Appl*, 8:95. https://doi.org/10.1038/s41377-019-0206-2

Berry MV, 1987. The adiabatic phase and Pancharatnam's phase for polarized light. *J Mod Opt*, 34(11):1401-1407. https://doi.org/10.1080/09500348714551321

Deng ZL, Cao YY, Li XP, et al., 2018. Multifunctional metasurface: from extraordinary optical transmission to extraordinary optical diffraction in a single structure. *Photon Res*, 6(5):443-450. https://doi.org/10.1364/prj.6.000443

Devlin RC, Khorasaninejad M, Chen WT, et al., 2016. Broadband high-efficiency dielectric metasurfaces for the visible spectrum. *Proc Nat Acad Sci USA*, 113(38):10473-10478. https://doi.org/10.1073/pnas.1611740113

Feng H, Li QT, Wan WP, et al., 2019. Spin-switched three-dimensional full-color scenes based on a dielectric metahologram. *ACS Photon*, 6(11):2910-2916. https://doi.org/10.1021/acsphotonics.9b01017

Georgi P, Wei QS, Sain B, et al., 2021. Optical secret sharing with cascaded metasurface holography. *Sci Adv*, 7(16): eabf9718. https://doi.org/10.1126/sciadv.abf9718

Guo ZM, Liu HH, Xiang LN, et al., 2020. Generation of perfect vortex beams with polymer-based phase plate. *IEEE Photon Technol Lett*, 32(10):565-568. https://doi.org/10.1109/lpt.2020.2985745

Hao X, Allgeyer ES, Lee DR, et al., 2021. Three-dimensional adaptive optical nanoscopy for thick specimen imaging at sub-50-nm resolution. *Nat Methods*, 18(6):688-693. https://doi.org/10.1038/s41592-021-01149-9

He X, Liu YJ, Ganesan K, et al., 2020. A single sensor based multispectral imaging camera using a narrow spectral band color mosaic integrated on the monochrome CMOS image sensor. *APL Photon*, 5(4):046104. https://doi.org/10.1063/1.5140215

Hell SW, Wichmann J, 1994. Breaking the diffraction resolution limit by stimulated emission: stimulated-emission-depletion fluorescence microscopy. *Opt Lett*, 19(11):780-782. https://doi.org/10.1364/ol.19.000780

Hu YF, Liu X, Jin MK, et al., 2021. Dielectric metasurface zone plate for the generation of focusing vortex beams. *PhotoniX*, 2(1):10. https://doi.org/10.1186/s43074-021-00035-z

Huang TY, Zhang DZ, Yoo S, et al., 2020. Reconfigurable multiwavelength fiber laser based on multimode interference in highly germanium-doped fiber. *Appl Opt*, 59(4): 1163-1168. https://doi.org/10.1364/ao.383627

Ikezawa S, Yamada R, Takaki K, et al., 2022. Micro-optical line generator metalens for a visible wavelength based on octagonal nanopillars made of single-crystalline silicon. *IEEE Sens J*, 22(15):14851-14861. https://doi.org/10.1109/jsen.2022.3186060

Jesacher A, Bernet S, Ritsch-Marte M, 2014. Broadband suppression of the zero diffraction order of an SLM using its extended phase modulation range. *Opt Expr*, 22(14): 17590-17599. https://doi.org/10.1364/oe.22.017590

Khorasaninejad M, Ambrosio A, Kanhaiya P, et al., 2016a. Broadband and chiral binary dielectric meta-holograms. *Sci Adv*, 2(5):e1501258. https://doi.org/10.1126/sciadv.1501258

Khorasaninejad M, Chen WT, Devlin RC, et al., 2016b. Metalenses at visible wavelengths: diffraction-limited focusing and subwavelength resolution imaging. *Science*, 352(6290): 1190-1194. https://doi.org/10.1126/science.aaf6644

Li Y, Liu SJ, Sun DQ, et al., 2021. Single-layer multitasking vortex-metalens for ultra-compact two-photon excitation STED endomicroscopy imaging. *Opt Expr*, 29(3):3795-3807. https://doi.org/10.1364/oe.416698

Liu MZ, Zhu WQ, Huo PC, et al., 2021. Multifunctional metasurfaces enabled by simultaneous and independent control of phase and amplitude for orthogonal polarization states. *Light Sci Appl*, 10(1):107. https://doi.org/10.1038/s41377-021-00552-3

Liu X, Peng YF, Tu SJ, et al., 2021. Generation of arbitrary longitudinal polarization vortices by pupil function manipulation. *Adv Photon Res*, 2(1):2000087. https://doi.org/10.1002/adpr.202000087

Liu X, Tu SJ, Kuang CF, et al., 2022. Calibration of phase-only liquid-crystal spatial light modulators by diffractogram analysis. *Opt Lasers Eng*, 156:107056. https://doi.org/10.1016/j.optlaseng.2022.107056

Ma JQ, Li Y, Yu QZ, et al., 2018. Generation of high-quality tunable Airy beams with an adaptive deformable mirror. *Opt Lett*, 43(15):3634-3637. https://doi.org/10.1364/ol.43.003634

Maguid E, Yulevich I, Veksler D, et al., 2016. Photonic spin-controlled multifunctional shared-aperture antenna array. *Science*, 352(6290):1202-1206. https://doi.org/10.1126/science.aaf3417

Mirhosseini M, Magaña-Loaiza OS, O'Sullivan MN, et al., 2015. High-dimensional quantum cryptography with twisted

light. *New J Phys*, 17(3):033033. https://doi.org/10.1088/1367-2630/17/3/033033

Mueller JPB, Rubin NA, Devlin RC, et al., 2017. Metasurface polarization optics: independent phase control of arbitrary orthogonal states of polarization. *Phys Rev Lett*, 118(11): 113901. https://doi.org/10.1103/PhysRevLett.118.113901

Ouadghiri-Idrissi I, Giust R, Froehly L, et al., 2016. Arbitrary shaping of on-axis amplitude of femtosecond Bessel beams with a single phase-only spatial light modulator. *Opt Expr*, 24(11):11495-11504. https://doi.org/10.1364/oe.24.011495

Richards B, Wolf E, 1959. Electromagnetic diffraction in optical systems, II. Structure of the image field in an aplanatic system. *Proc Roy Soc A Math Phys Eng Sci*, 253(1274): 358-379. https://doi.org/10.1098/rspa.1959.0200

Ruffato G, Massari M, Romanato F, 2014. Generation of high-order Laguerre–Gaussian modes by means of spiral phase plates. *Opt Lett*, 39(17):5094-5097. https://doi.org/10.1364/ol.39.005094

Sasaki H, Yamamoto K, Wakunami K, et al., 2014. Large size three-dimensional video by electronic holography using multiple spatial light modulators. *Sci Rep*, 4:6177. https://doi.org/10.1038/srep06177

Sell D, Yang JJ, Doshay S, et al., 2017. Periodic dielectric metasurfaces with high-efficiency, multiwavelength functionalities. *Adv Opt Mater*, 5(23):1700645. https://doi.org/10.1002/adom.201700645

Shi ZJ, Khorasaninejad M, Huang YW, et al., 2018. Single-layer metasurface with controllable multiwavelength functions. *Nano Lett*, 18(4):2420-2427. https://doi.org/10.1021/acs.nanolett.7b05458

Shrestha S, Overvig AC, Lu M, et al., 2018. Broadband achromatic dielectric metalenses. *Light Sci Appl*, 7:85. https://doi.org/10.1038/s41377-018-0078-x

Spägele C, Tamagnone M, Kazakov D, et al., 2021. Multifunctional wide-angle optics and lasing based on supercell metasurfaces. *Nat Commun*, 12(1):3787. https://doi.org/10.1038/s41467-021-24071-2

Yang WH, Xiao SM, Song QH, et al., 2020. All-dielectric metasurface for high-performance structural color. *Nat Commun*, 11(1):1864. https://doi.org/10.1038/s41467-020-15773-0

Yu XM, Todi A, Tang HM, 2018. Bessel beam generation using a segmented deformable mirror. *Appl Opt*, 57(16): 4677-4682. https://doi.org/10.1364/ao.57.004677

Zhang WY, Song HY, He X, et al., 2021. Deeply learned broadband encoding stochastic hyperspectral imaging. *Light Sci Appl*, 10(1):108. https://doi.org/10.1038/s41377-021-00545-2

Zhao MX, Chen MK, Zhuang ZP, et al., 2021. Phase characterisation of metalenses. *Light Sci Appl*, 10(1):52. https://doi.org/10.1038/s41377-021-00492-y

Zheng JY, He X, Beckett P, et al., 2021. Dichroic circular polarizers based on plasmonics for polarization imaging applications. *Nanomaterials*, 11(8):2145. https://doi.org/10.3390/nano11082145

List of supplementary materials